those obtained from magnetoacoustic measurements. No other sheet of the magnesium Fermi surface, however, satisfies the inversion criteria and for these one must rely on area calculations based on some simple Fermi surface models. One generally assumes that the model is valid if the calculated cross-sectional area branches agree reasonably well with experimental data. The problem with most model calculations, however, is that this process is by no means unique. The best model calculations for simple metals, i.e., those with tightly bound inert-gas-like cores, seems to be those based on the pseudopotential model Hamiltonian.

The DHVA data reported here contain nearly complete information on all sheets of the Fermi surface except the small first-band cap. If we describe the area branches in terms of solid angles of $\mathbf{k}$ vectors at the Fermi surface, this data covers over 90% of the total Fermi surface. In the following paper, we will use this data together with that presented in I to obtain Fermi surface models using the pseudopotential approximation for the band structure. For this reason we have made no attempt in this paper to obtain quantitative agreement with any simple model. We note, however, that qualitatively the data are in excellent agreement with the predictions of the single-OPW model[2] and had we made the comparison, we would have found that the two-OPW model[1] also gave reasonable quantitative agreement.

PHYSICAL REVIEW VOLUME 162, NUMBER 3 15 OCTOBER 1967

The Fermi Surface of Magnesium III: Local and Nonlocal Pseudopotential Band Structure Models for Magnesium*

J. C. KIMBALL† AND R. W. STARK‡
Department of Physics and James Franck Institute, The University of Chicago, Chicago, Illinois
AND
F. M. MUELLER
Argonne National Laboratory, Argonne, Illinois
(Received 17 April 1967)

Extensive de Haas–van Alphen cross-sectional areas and magnetoacoustic calipers for the magnesium Fermi surface were used to generate local- and nonlocal-pseudopotential model Hamiltonians. Both models yielded a good representation of the Fermi surface. Small but significant deviations from experimental data could not be eliminated using the local model, but these were eliminated with the nonlocal model. The values of the local-pseudopotential Fourier coefficients obtained were $U_{10\bar{1}0}=+0.014$ Ry, $U_{0002}=+0.026$ Ry, $U_{10\bar{1}1}=+0.036$ Ry, and $U_{10\bar{1}2}=+0.058$ Ry. The variational parameters for the nonlocal pseudopotential were the Fourier coefficients of the self-consistent ion-core potential $V(\mathbf{r})$. The values obtained for these were $V_{10\bar{1}0}=-0.440$ Ry, $V_{0002}=-0.412$ Ry, $V_{10\bar{1}1}=-0.386$ Ry, and $V_{10\bar{1}2}=-0.299$ Ry.

INTRODUCTION

THIS paper is the third in a series devoted to the experimental and theoretical determination of the band structure of magnesium. The first paper[1] in this series, which will henceforth be referred to as I, dealt with extensive magnetoacoustic investigations; the second paper,[2] henceforth to be referred to as II, described the results of extensive de Haas–van Alphen investigations. In general, the data contained in I and II have been found to be in *qualitative* agreement with the single-OPW model[3] and Falicov's first principles OPW calculations (OPW = orthogonalized plane wave).[4] The agreement with Falicov's model is in fact within his estimated error of about 5% of the Fermi energy E_F; the principal part of this error results from uncertainties in the electron correlation and exchange energies. The available experimental data is sensitive to variations of about 0.1% in E_F; current first-principles calculations can not approach this accuracy. Thus, in order to take full advantage of these data (which are limited to the energy contour E_F) in gaining insight into the magnesium band structure, one must use a semiempirical model Hamiltonian such as those based on pseudopotential theory.[5,6]

This approach has the dual advantage of acting as an interpolation procedure whereby limited experimental information can be used to generate the entire Fermi surface, and of generating $E(\mathbf{k})$ bands for $E(\mathbf{k})\neq E_F$.

* Work supported in part by the Army Research Office (Durham), the Alfred P. Sloan Foundation, the Advanced Research Projects Agency, and the U. S. Atomic Energy Commission.
† National Science Foundation Predoctoral Fellow.
‡ Alfred P. Sloan Research Fellow.
[1] J. B. Ketterson and R. W. Stark, Phys. Rev. **156**, 748 (1967).
[2] R. W. Stark, Phys. Rev. (preceding article).
[3] W. A. Harrison, Phys. Rev. **118**, 1190 (1960).
[4] L. M. Falicov, Phil. Trans. **A255**, 55 (1962).
[5] W. A. Harrison, *Pseudopotentials in the Theory of Metals* (W. A. Benjamin, Inc., 1966), and enclosed references.
[6] J. M. Ziman, Advan. Phys. **13**, 89 (1964).

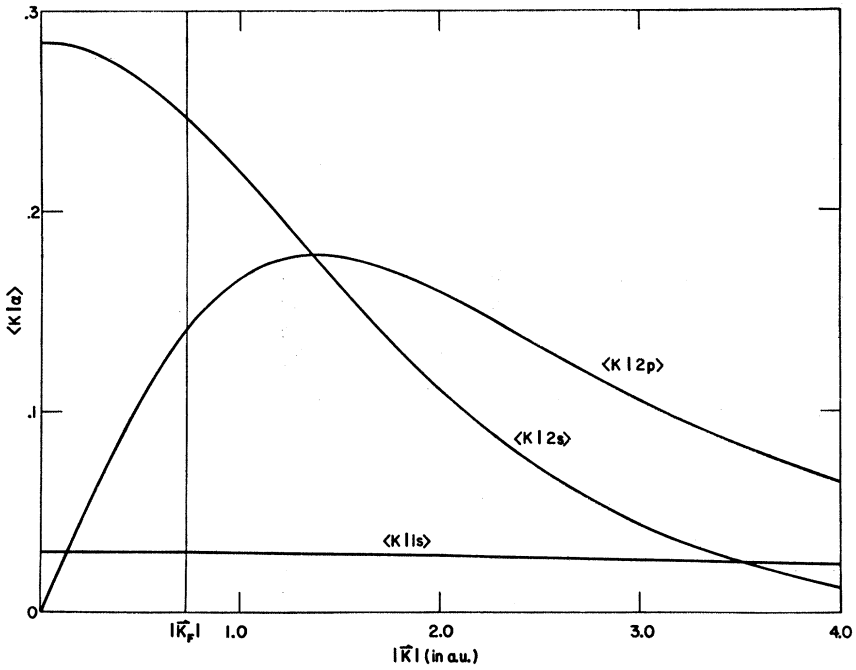

FIG. 1. The Fourier transforms of the radial portion of the 1s, 2s, and 2p atomic wave functions. A factor of $[(2l+1)/4\pi]^{1/2}$ has been included in the numerical values.

THEORY

The pseudopotential model was originally derived from the one-electron crystalline wave equation by expanding the eigenfunctions in orthogonalized plane waves (OPW's) and transposing the orthogonalization terms to the left side of the equation. This yielded the equation [in atomic units, (a.u.)]

$$\mathcal{H}\varphi_{\mathbf{k}}(\mathbf{r})=\{-\nabla^2+U(\mathbf{r},\mathbf{k})\}\varphi_{\mathbf{k}}(\mathbf{r})=E_{\mathbf{k}}\varphi_{\mathbf{k}}(\mathbf{r}), \quad (1a)$$

$$U(\mathbf{r},\mathbf{k})=V(\mathbf{r})+\sum_{\alpha}(E_{\mathbf{k}}-E_{\alpha})|\alpha\rangle\langle\alpha|, \quad (1b)$$

where $V(\mathbf{r})$ is the self-consistent periodic potential of the ion cores and the $|\alpha\rangle$ and E_α are core states and core eigenvalues, respectively. In this representation the pseudo-wave-function $\varphi_{\mathbf{k}}(\mathbf{r})$ became a linear combination of plane waves, i.e.,

$$\varphi_{\mathbf{k}}(\mathbf{r})=\sum_{\mathbf{G}}A_{\mathbf{G}}|\mathbf{k}+\mathbf{G}\rangle, \quad (2)$$

where $\mathbf{G}$ label the reciprocal lattice vectors. The pseudopotential $U(\mathbf{r},\mathbf{k})$ resulted from the cancellation of the large attractive $V(\mathbf{r})$ by the repulsive core terms and hence was much more smoothly varying than $V(\mathbf{r})$. The band-structure problem thus became one of treating plane-wave states in a fairly smoothly varying but nonlocal potential. The pseudopotential $U(\mathbf{r},\mathbf{k})$ was often approximated by a local potential to give

$$U(\mathbf{r},\mathbf{k})=U(\mathbf{r})=\sum_{\mathbf{G}}U_{\mathbf{G}}S_{\mathbf{G}}\,e^{i\mathbf{G}\cdot\mathbf{r}}. \quad (3)$$

In this paper we present results based on calculations using both this local approximation and a simple nonlocal formulation of the pseudopotential.

A typical matrix element in the local approximation is

$$\langle\mathbf{k}_i|\mathcal{H}|\mathbf{k}_j\rangle=k^2\delta_{\mathbf{k}_i,\mathbf{k}_j}+U_{\mathbf{k}_i-\mathbf{k}_j}S_{\mathbf{k}_i-\mathbf{k}_j}, \quad (4)$$

where $U_{\mathbf{k}_i-\mathbf{k}_j}$ is the appropriate Fourier coefficient in Eq. (3) and $S_{\mathbf{k}_i-\mathbf{k}_j}$[7] is the structure factor. The variable parameters for this model are the U_G's where $\mathbf{G}=\mathbf{k}_i-\mathbf{k}_j$. Since the magnesium Fermi surface intersects three Brillouin zone planes for which the structure factor is nonvanishing, only three of the local Fourier expansion coefficients will be of first-order importance. These are the $U_{10\bar{1}0}$, U_{0002}, and $U_{10\bar{1}1}$ coefficients listed in order of increasing $|\mathbf{G}|$. Estimates of these coefficients were given in I.[7] Of the remaining coefficients, we found $U_{10\bar{1}2}$ was the only one which had a significant effect on the Fermi surface. Initially, all four of these coefficients were determined independently; they were found to fit the functional form

$$U_G=A(|\mathbf{G}|-G_0)\exp[-B(|\mathbf{G}|-G_0)]. \quad (5)$$

The final local pseudopotential calculations were made using this general expression for all U_G.

The nonlocal pseudopotential model which we have used is defined by Eq. (1b). The $|\alpha\rangle$ and E_α are approximated by their corresponding atomic eigenfunctions and eigenvalues.[8] In principle, the atomic E_α should

[7] $S_G=\cos(2\pi\mathbf{G}\cdot\boldsymbol{\tau}/2)$, where $\boldsymbol{\tau}$ is defined in I. Note that the structure factor used in I was a factor of 2 too large so that the estimates given there for the local pseudopotential coefficients are a factor of 2 too small.

[8] F. Herman and S. Skillman, *Atomic Structure Calculations* (Prentice-Hall, Inc., Englewood Cliffs, New Jersey, 1963).

change, by a small amount (~ -0.25 Ry), the core shift[9] in the crystalline state. However, our calculations appeared to be insensitive to these small shifts. A typical nonlocal matrix element in this calculation is

$$\langle \mathbf{k}_i|\mathcal{H}|\mathbf{k}_j\rangle = k^2\delta_{\mathbf{k}_i,\mathbf{k}_j}+[V_{\mathbf{k}_i-\mathbf{k}_j}+(E_\mathbf{k}-E_{1s})\{k_i|1s\} \times\{1s|k_j\}+(E_\mathbf{k}-E_{2s})\{k_i|2s\}\{2s|k_j\} +(E_\mathbf{k}-E_{2p})\{k_i|2p\}\{2p|k_j\}\times\cos\Theta]S_{\mathbf{k}_i-\mathbf{k}_j}, \quad (6)$$

where $V_{\mathbf{k}_i-\mathbf{k}_j}$ is the coefficient of the Fourier transform of the self-consistent ion-core potential, $\{k|\alpha\}$[10] is the radial portion of the Fourier transform of $|\alpha\rangle$ times the factor $[(2l+1)/4\pi]^{1/2}$ as shown in Fig. 1, and Θ is the angle between $\mathbf{k}_j$ and $\mathbf{k}_i$. The only adjustable parameter in Eq. (6) is $V_{\mathbf{k}_i-\mathbf{k}_j}$.

Because this matrix element is nonlocal, it will vary with the vector $\mathbf{k}_i$, even though the difference $\mathbf{k}_i-\mathbf{k}_j=\mathbf{G}$ remains unchanged or even if $\mathbf{k}_i$ follows a constant energy contour. As an example of the variations which occur in this matrix element with changes in $\mathbf{k}_i$, consider the situation shown in Fig. 2(a). We will follow the changes in the matrix element $\langle \mathbf{k}_i|\mathcal{H},\mathbf{k}_j\rangle$ for $\mathbf{k}_i-\mathbf{k}_j=\mathbf{G}_{0002}$. In Fig. 2(a) the vector $\mathbf{k}_i$ traverses the path A-B-C-Γ. Path A-B lies in the (0002) zone plane. The point labeled A represents the midpoint of the third band lens; the point labeled B is the intersection of the lens with the (0002) plane. Path B-C follows the constant energy contour $E_\mathbf{k}=E_F$. Path C-Γ completes the circuit. Note that on this last path the angle between $\mathbf{k}_i$ and $\mathbf{k}_j$ remains fixed at a constant value of π. The values of $\langle \mathbf{k}_i|\mathcal{H}|\mathbf{k}_j\rangle$ corresponding to points along this path are shown as the solid curve in Fig. 2(b). The constant local pseudopotential matrix element is shown there as the dashed curve.

In this nonlocal calculation we set $\langle \mathbf{k}_i|\mathcal{H}|\mathbf{k}_j\rangle=0$ for $|\mathbf{k}_i-\mathbf{k}_j|$ greater than the length of the $[10\bar{1}2]$ reciprocal-lattice vector. Note that in this formulation $\mathcal{H}(\mathcal{E}_\mathbf{k})\varphi_\mathbf{k}(\mathbf{r})=\mathcal{E}_\mathbf{k}\varphi_\mathbf{k}(\mathbf{r})$, so that the eigenvalue $\mathcal{E}_\mathbf{k}$ must be determined self-consistently; for purposes of comparison with experimental data, $\mathcal{E}_\mathbf{k}=E_F$.

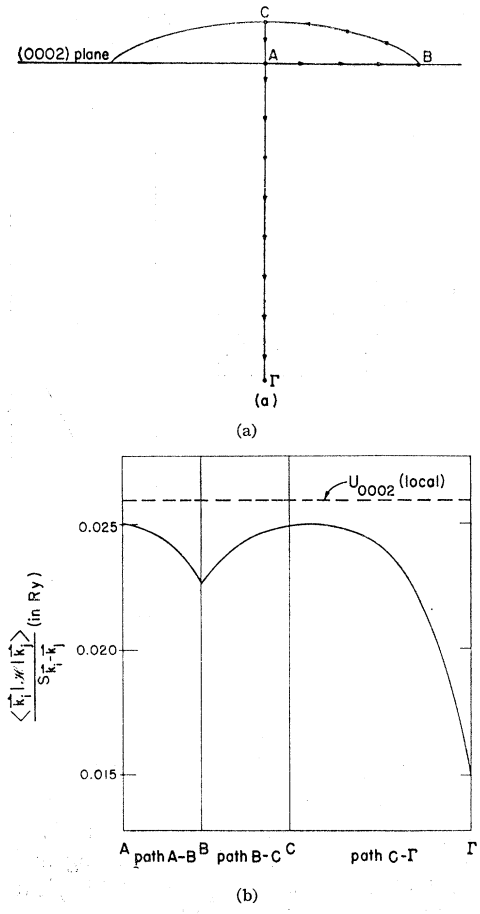

FIG. 2. The $\mathbf{k}$ dependence of a typical nonlocal matrix element $\langle \mathbf{k}_i|\mathcal{H}|\mathbf{k}_j\rangle$ with $\mathbf{k}_i-\mathbf{k}_j=\mathrm{G}_{0002}$. (a) Variation of $\mathbf{k}_i$; path A–B: in the (0002) zone plane; path B–C: on the constant energy surface E_F of the lens; path C–Γ: along the line for which $\mathbf{k}_i$ and $\mathbf{k}_j$ are antiparallel $[\theta=\pi$, see Eq. (6)]. (b) The value of $\langle \mathbf{k}_i|\mathcal{H}|\mathbf{k}_j\rangle$ for $\mathbf{k}_i$ constrained to the path shown in (a).

The experimental data give the following information about the Fermi surface: connectivity,[11] surface calipers,[1] and extremal areas.[2] The latter information is the most complete and the most accurate. Because most of the sheets of the surface do not have sufficient symmetry to allow a direct conversion of area to radii,[12] it was necessary to adopt the following iterative procedure in calculating both the local and the nonlocal band structures:

(1) Initial values on symmetry lines of 11 *select* points (see Table I), $\mathbf{k}_i$, on various sheets of the Fermi

[9] P. J. Lin and J. C. Phillips, Advan. Phys. **14**, 257 (1965).

[10] The core states $|\alpha\rangle$ are expressed in terms of spherical harmonics:

$$|\alpha\rangle=\frac{P_{nl}(r)}{r}Y_{lm}(\theta,\varphi),$$

where $P_{nl}(r)$ is tabulated in Ref. 8.

$$\langle \mathbf{k}|\alpha\rangle = V^{-1/2}\int e^{-i\mathbf{k}\cdot\mathbf{r}}P_{nl}(r)Y_{lm}(\theta,\varphi)r\,dr d\Omega,$$

where V is the volume of the Wigner-Seitz cell enclosing *one* ion and $d\Omega$ is the element of solid angle. Hence,

$$\langle \mathbf{k}|\alpha\rangle=\frac{4\pi}{V^{1/2}}iY_{lm}(\hat{k})\int_0^\infty P_{nl}(r)j_l(kr)rdr$$
$$=Y_{lm}(\hat{k})F_{nl}(|\mathbf{k}|),$$

where we now define $F_{nl}(|\mathbf{k}|)$ to be the radial portion of the Fourier transform. By use of the addition theorem all terms for a given n and l can be combined to yield

$$\sum Y_{lm}^*(\hat{k})Y_{lm}(\hat{k})=\frac{2l+1}{4\pi}P_l(\cos\Theta),$$

where Θ is defined by $\hat{k}\cdot\hat{k}'=\cos\Theta$. Thus, for a given n and l

$$\sum_m \langle \mathbf{k}|\alpha\rangle\langle\alpha|\mathbf{k}'\rangle=\frac{2l+1}{4\pi}F_{nl}(|\mathbf{k}|)F_{nl}(|\mathbf{k}'|)P_l(\cos\Theta)$$
$$=\{k|\alpha\}\{\alpha|k'\}P_l(\cos\Theta),$$

where now $\alpha=1s,\ 2s,\ 2p$.

[11] R. W. Stark, T. G. Eck, and W. L. Gordon, Phys. Rev. **133**, A443 (1964).

[12] F. M. Mueller, Phys. Rev. **148**, 636 (1966).

TABLE I. Experimental calipers used to determine the Fourier coefficients.

Number	Symbol[a]	Sheet	Fourier coefficients most influenced by
1	$k^{\Gamma K}$	Lens	
2	$k^{\Gamma M}$	Lens	
3	$k^{\Gamma A}$	Lens	[0002]
4	$k_{\text{in}}{}^{\Gamma M}$	Monster	
5	k^{LH}	Butterfly	
6	$k^{L\Sigma'}$	Butterfly	[10$\bar{1}$1]
7	$k^{\Sigma' L}$	Monster	
8[b]	$k_{\text{out}}{}^{\Gamma K}$	Monster	
9[b]	$k^{K\Gamma}$	Cigar	[10$\bar{1}$0]
10[b]	k^{KH}	Cigar	
11[b]	$k_{\text{out}}{}^{\Gamma M}$	Monster	

[a] Notation as defined in I. Caliper dimensions are given in Table III.
[b] Strongly influenced in second order by (10$\bar{1}$1).

surface were obtained from measured and deduced experimental calipers.[2,11]

(2) Using these points, the model-band-structure parameters were found by minimalization of η, where

$$\eta^2=(1/11)\sum_i[E(\mathbf{k}_i)-E_F]^2$$

and

$$E_F=(1/11)\sum_i E(\mathbf{k}_i). \tag{7}$$

(3) These model-band-structure parameters were used to calculate several selected extremal areas.

(4) Based on differences between the calculated and experimental areas, the 11 caliper points were moved in direction and magnitude to minimize the deviation in the areas. (These changes were always within the experimental error of the initial calipers and remained bound to the symmetry lines.)

(5) Steps 2, 3, and 4 were repeated until area deviations were minimal.

Table I lists the 11 points which were used to obtain a rapidly converging set of values for both the local and nonlocal pseudopotentials. The Fourier coefficients indicated for each of the three groups were those which had first-order importance on the various calipers.

The final calculations were made using a ten plane wave expansion for $\varphi_{\mathbf{k}}(\mathbf{r})$ [Eq. (2)]. The convergence error associated with this secular equation was estimated to be about 1.5×10^{-3} Ry by a further expansion of $\varphi_{\mathbf{k}}(\mathbf{r})$ to about 25 plane waves. The integration errors in area calculations using these model Hamiltonians were smaller than 0.5%. A typical grid of calculated points is shown in Fig. 3 for the area determination of one cross section of the third-band cigar.

Table II lists the final values for the Fourier coefficients for both the local and nonlocal pseudopotential models. Also listed are the values of E_F measured with respect to the bottom of the conduction band for each model, the values of A, B, and G_0 in Eq. (5), and the values of E_F-E_α in Eq. (6). The signs of these coefficients were uniquely determined by the calculational procedure described above. This was because the signs are determined by second-order effects whose magnitudes were much larger than the truncation error. The Fourier coefficients of $V(\mathbf{r})$ listed in Table II should not be considered to be unique. These are determined primarily by our choice of the core eigenfunctions and eigenvalues[8] and would be modified by a different set, although the consistency obtained between various atomic calculations would seem to indicate that any modifications would be small.

It is interesting to compare our local pseudopotential coefficients with the predictions of the model potential of Heine and Abarenkov.[13] This comparison, as shown in Fig. 4, indicates that for magnesium the model potential yields a form factor which is in surprisingly good agreement with our empirical parameters.

The variable parameters used in the nonlocal pseudopotential calculation were the Fourier coefficients of the self-consistent ion-core potential $V(\mathbf{r})$. Thus, these should be comparable with the first-principles potential which Falicov used in his calculation.[4] The solid curve

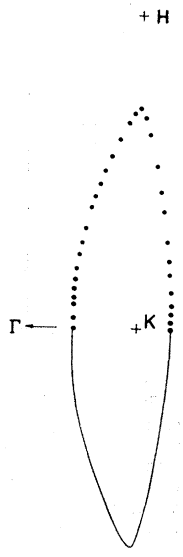

FIG. 3. Typical grid of Fermi-surface points calculated to determine the cross-sectional area of the cigar in the ΓKHA plane of the Brillouin zone.

TABLE II. Fourier coefficients of phenomenological potentials (in rydbergs).

Local Pseudopotential:

$U_G=A(G-G_0)e^{-B(G-G_0)}$

$A=+0.215$	$B=1.355$	$G_0=1.133$
$U_{10\bar{1}0}=+0.014$		$U_{10\bar{1}1}=+0.036$
$U_{0002}=+0.026$		$U_{10\bar{1}2}=+0.058$
	$E_F=0.522$[a]	
$V_{10\bar{1}0}=-0.440$		$V_{10\bar{1}1}=-0.386$
$V_{0002}=-0.412$		$V_{10\bar{1}2}=-0.299$
	$V_{0000}\approx-0.8$[b]	
	$E_F=0.518$[a]	
$E_F-E_{1s}=94.11$	$E_F-E_{2s}=6.49$	$E_F-E_{2p}=4.05$

[a] Measured relative to Γ_1^+.
[b] Calculated using the experimental value of the work function.

[13] A. O. E. Animalu and V. Heine, Phil. Mag. 12, 1249 (1965).

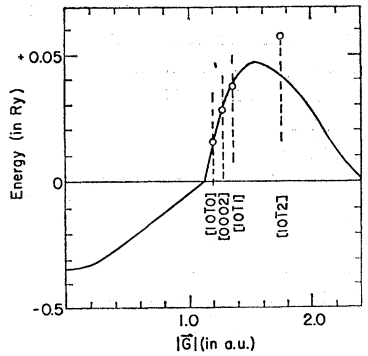

FIG. 4. The [10$\bar{1}$0], [0002], [10$\bar{1}$1], and [10$\bar{1}$2] Fourier coefficients of the local pseudopotential. The solid curve is the form factor for the magnesium model potential of Heine and Abarenkov calculated by Animalu and Heine (Ref. 12). Note that the positive scale is enlarged by a factor of 10 compared with the negative scale.

in Fig. 5 shows the Fourier transform of Falicov's first-principles potential. Compared with this are the four empirically determined Fourier coefficients of $V(\mathbf{r})$ as well as a rough estimate of the [0000] coefficient. The striking feature here is that the empirical coefficients appear to be about 0.1 Ry more negative than the first-principles potential.

A direct comparison between the size of the Fourier coefficients of $U(\mathbf{r})$ and $V(\mathbf{r})$ for each of the four shortest reciprocal-lattice vectors can be made in Table II. Note that the cancellation of $V(\mathbf{r})$ by the core terms is complete to within about 10%.

Even though our calculated bands are degenerate across the AHL plane of the Brillouin zone, we will use the single-zone scheme representation in the following discussion. This degeneracy is removed by the effects of spin-orbit coupling[14] across this entire plane with the exception of the AL line. Since spin-orbit effects are considerably smaller than our truncation error, they were not included explicitly in the calculation.

DISCUSSION OF THE MODEL BAND STRUCTURES

The accuracy with which these band-structure models represent the experimental data is illustrated in Tables III and IV. Table III lists the important magnetoacoustic Fermi-surface calipers reported in I together with those calculated from each of our model Hamiltonians. In all cases except one, the calculated calipers for both models are within the experimental error of the magnetoacoustic calipers. The one discrepancy occurs for the fourth-band electron pocket and in this case the discrepancy almost certainly results from an error in the initial assignment of the magnetoacoustic caliper.

The very small differences between the calipers calculated for our local and nonlocal models are an indication of the small error resulting from the local approximation. This illustrates that the nonlocal corrections are essentially of second-order importance.

[14] L. M. Falicov and M. L. Cohen, Phys. Rev. **130**, 92 (1963).

TABLE III. Calculated and experimental dimensions (a.u.).

Sheet	Dimension	Measured	Experimental	Local	Nonlocal
Monster	Inside	$K_{\text{in}}{}^{\Gamma K}$	0.370±0.007	0.3706	0.3705
		$K_{\text{in}}{}^{\Gamma M}$	0.370±0.007	0.3705	0.3706
	Outside	$K_{\text{out}}{}^{\Gamma K}$	0.622±0.009	0.6284	0.6292
		$K_{\text{out}}{}^{\Gamma M}$	0.476±0.008	0.4706	0.4694
	Waist	$C_{\text{waist}}{}^{\Gamma M}$	0.100±0.002	0.1001	0.0988
		$K_{\text{waist}}{}^{\Sigma' L}$	0.064±0.002	0.0639	0.0615
Lens		$K_{\text{lens}}{}^{\Gamma A}$	0.080±0.003	0.0825	0.0801
		$K_{\text{lens}}{}^{\Gamma K}$	0.312±0.006	0.3114	0.3142
		$K_{\text{lens}}{}^{\Gamma M}$	0.312±0.006	0.3125	0.3143
Cigar		$C_{\text{cigar}}{}^{\Gamma KM}$	0.100±0.005	0.0990	0.0991
		$K_{\text{cigar}}{}^{K\Gamma}$	≈0.067	0.0634	0.0647
		$K_{\text{cigar}}{}^{KM}$	≈0.033	0.0356	0.0345
Butterfly		$K_{BF}{}^{LH}$	0.184±0.002	0.1834	0.1834
		$K_{BF}{}^{L\Sigma'}$	0.206±0.016	0.1816	0.1823
Fourth-band pocket		$K_{\text{P}}{}^{LM}$	0.043±0.035	0.0729	0.0715
Cap		$K_{\text{cap}}{}^{HA}$		0.0308	0.0281
		$K_{\text{cap}}{}^{HK}$		0.0832	0.0753
		$K_{\text{cap}}{}^{HL}$		0.0421	0.0383

Table IV lists the important cross-sectional areas of the Fermi surface reported in II together with those calculated from our models. The local model yields good agreement with the experimental data on all sheets of the Fermi surface with the exception of the second-band monster which appears to be a bit too large. It should be noted that these discrepancies, although significant, are only about twice as large as our estimated truncation error. It was not found to be possible to improve the accuracy of the local model by further variations of the Fourier coefficients of the pseudopotential since a model yielding better agreement with the monster always led to poorer agreement on other sheets of the Fermi surface.

The cross-sectional areas calculated for the nonlocal model yield better agreement with the experimental

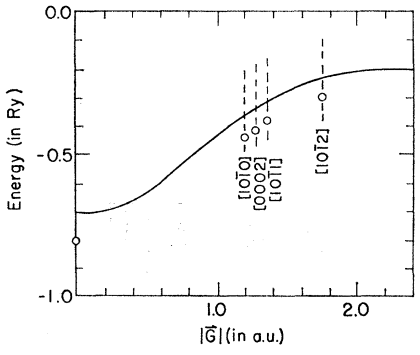

FIG. 5. The [10$\bar{1}$0], [0002], [10$\bar{1}$1] and [10$\bar{1}$2] Fourier coefficients of $V(\mathbf{r})$ obtained for the nonlocal pseudopotential. The [0000] coefficient was estimated to ±0.1 Ry from the experimental value of the work function. The solid curve is the form factor for Falicov's (Ref. 4) calculated shielded potential. The apparent constant differences between these two can be interpreted as a core shift.

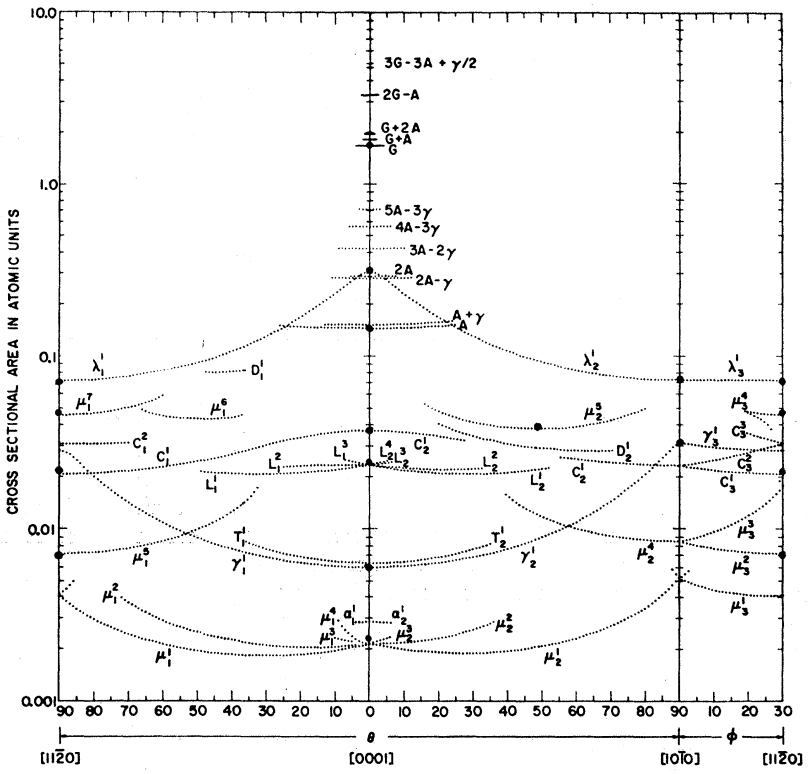

FIG. 6. Several de Haas–van Alphen extremal area branches for magnesium reported in the preceding article. The large dots are the values calculated for these branches using the nonlocal pseudopotential.

data. In all cases the differences were within the truncation error. In this sense the nonlocal model is a definite improvement over the local model. Figure 6 shows the de Haas–van Alphen area branches reported in II together with those points calculated for the nonlocal model. The agreement between the specific calculated points and the pertinent area branches validates the orbit assignments given in II for these branches.

For a pseudopotential model, the cross sections of the Fermi surface should be similar to the single-OPW model. Since our nonlocal model yields the better representation, we present only the nonlocal cross sections. These as well as the corresponding single-OPW cross sections are shown in Fig. 7 and 8 for the major symmetry planes in the Brillouin zone. These figures show that the magnesium Fermi surface is strikingly free-electron-like. One should note in Fig. 7 that the [10$\bar{1}$0] band gap separating the monster and the cigar is quite small and, in fact, vanishes at one point. At that point there is an accidental degeneracy between

TABLE IV. Calculated and experimental cross-sectional areas.

Sheet	θ Coordinates of H[a]	Symbol[b]	Areas (10^2 a.u.) A_{local}	$\frac{A_{\text{local}}-A_{\text{exp}}}{A_{\text{exp}}}$	A_{exp}	$\frac{A_{\text{nonlocal}}-A_{\text{exp}}}{A_{\text{exp}}}$	A_{nonlocal}
Monster	0	μ_1^1	0.296	37.7%	0.215	0.5%	0.216
	90	μ_1^6	0.746	3.5%	0.721	1.9%	0.707
	48.5	μ_2^5	3.96	4.2%	3.80	1.8%	3.87
	90	μ_2^7	4.70	4.0%	4.52	−0.9%	4.48
Cigar	0	γ_1^1	0.610	2.0%	0.598	2.3%	0.612
	90	γ_2^1	3.10	−1.0%	3.13	0.3%	3.14
Lens	0°	λ_1^1	30.6	−0.6%	30.8	0.3%	30.9
	90°	λ_1^1	7.30	0.6%	7.26	0.8%	7.32
	90	λ_2^1	7.30	0.4%	7.27	0.8%	7.34
Clam-	0	L_1^1	2.36	1.0%	2.34	−0.4%	2.33
Butterfly	0	C_1^1	3.70	−0.5%	3.72	−1.1%	3.68
	90	C_1^1	2.07	0.5%	2.08	−1.0%	2.06
Breakdown	0	G	167.0	0.0%	167.0	0.0%	167.0
Orbits	0	A	14.5	0.7%	14.4	0.7%	14.5

[a] The subscript number on each area symbol refers to the crystallographic plane containing **H** as defined in II. The (10$\bar{1}$0) plane is designated by 1, the (11$\bar{2}$0) plane is designated by 2, and the (0001) plane is designated by 3.
[b] As defined in II.

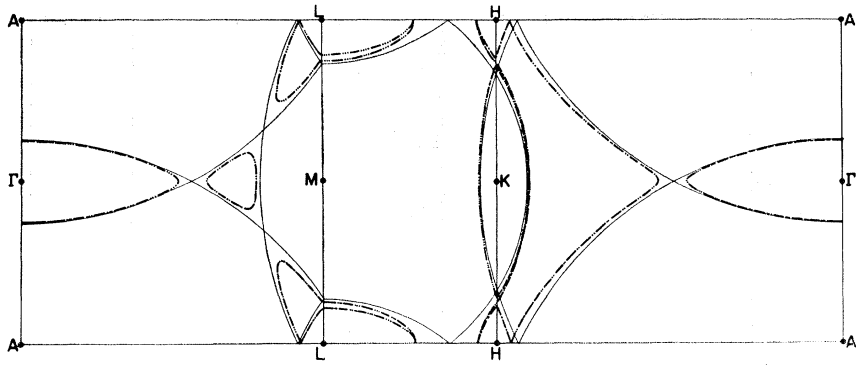

FIG. 7. Cross sections of the nonlocal pseudopotential Fermi surface in the unfolded zone scheme. The ., .., ..., and .... contours refer to the first, second, third, and fourth bands, respectively.

the two bands. Had we included spin-orbit coupling, this degeneracy would have been removed. The important point here is that the energy gap separating a large segment of these two sheets of the Fermi surface is quite small both in the ΓKM plane and near the tip of the cigar, and hence explains, via magnetic breakdown, both the giant orbit and trifoliate orbit reported in II (the G and T branches, respectively). In addition, Fig. 4 also shows that the $[10\bar{1}0]$ gap between the third-band butterfly and the fourth-band electron pocket vanishes by symmetry along the HL line and is small in the immediate vicinity of this line. Hence, magnetic breakdown across this gap generates the L branches reported in II.

The $\mathcal{E}(\mathbf{k})$ bands were calculated iteratively for the nonlocal model. These bands which are shown in Fig. 9 exhibit accidental degeneracies at several points. The $\mathcal{E}(\mathbf{k})$ bands were also calculated for the local model; these would appear, on the same scale as those shown in Fig. 9, to be very similar to the nonlocal bands. The difference $\mathcal{E}(\mathbf{k})_{\text{nonlocal}}-\mathcal{E}(\mathbf{k})_{\text{local}}$ is shown in Fig. 10. The tendency of this difference to become increasingly negative as the energy is increased reflects the fact that the nonlocal bands are generally slightly flatter. The undulating character of the difference reflects the $\mathbf{k}$ dependence of the nonlocal pseudopotential. It is interesting to note that the slope $\text{grad}_{\mathbf{k}}\mathcal{E}(\mathbf{k})$ of our bands is, on the average, about 40% smaller than Falicov obtained.[4] This apparently results from the Bohm-Pines correction, since the band energies without this "correction" which he quotes agree more closely with those shown in Fig. 9. This slope does not necessarily reflect upon the accuracy with which one can determine the Fermi surface but it does strongly influence the accuracy

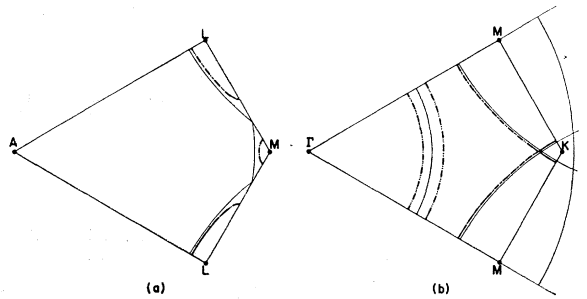

FIG. 8. Cross section of the nonlocal pseudopotential Fermi surface in the ΓKM and AHL planes of the Brillouin zone. The band notation is the same as that in Fig. 7.

TABLE V. Calculated and experimental cyclotron masses.

Sheet	θ coordinate of H	Symbol	m_{local}	Free-electron mass equals one $\frac{m_{\text{exp}}-m_{\text{local}}}{m_{\text{local}}}$	m_{exp}	$\frac{m_{\text{exp}}-m_{\text{OPW}}}{m_{\text{OPW}}}$	m_{OPW}
Monster	0°	μ_1^1	0.084	31.0%	0.11 ±0.01	29.4%	0.085
	90°	μ_1^5	0.104	32.7%	0.138±0.004	28.9%	0.107
	49°	μ_2^5	0.252	31.0%	0.33 ±0.01	27.4%	0.259
Cigar	0°	γ_1^1	0.078	28.2%	0.100±0.002	25.0%	0.080
	90°	γ_2^1	0.320	18.7%	0.38 ±0.05	21.7%	0.312
Lens	0°	λ_1^1	1.11				1.15
	90°	λ_2^1	0.323	30.0%	0.42 ±0.01	26.5%	0.332
	90°	λ_1^1	0.325	29.2%	0.42 ±0.01	24.6%	0.337
Breakdown	90°	C_1^1	0.241	32.8%	0.32 ±0.01	31.1%	0.244
Orbits	0°	G	1.11	26.1%	1.40 ±0.05	20.6%	1.16
	0°	A	0.418	31.6%	0.55 ±0.02	25.0%	0.44
Limiting point	0°		1.01	32.3%	1.33	25.5%	1.06
				Average	Standard Deviation	Average	Standard Deviation
				29.4%	3.9%	26.0%	3.0%

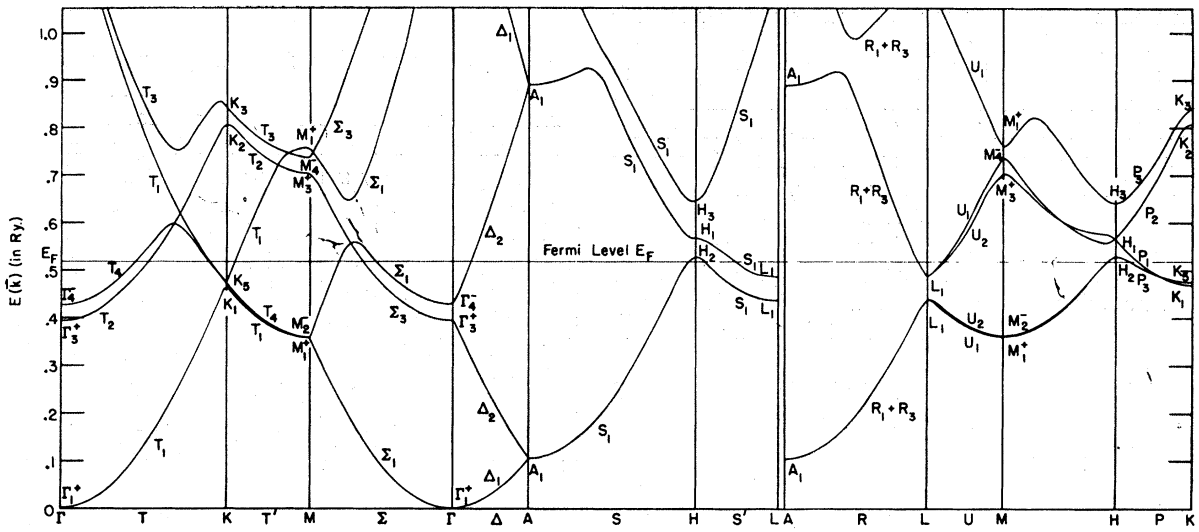

FIG. 9. The lowest energy bands along the major symmetry lines of the Brillouin zone for the nonlocal pseudopotential model.

with which one can calculate dynamical effects such as cyclotron masses.

We have used both the local and nonlocal models to calculate the cyclotron masses on those orbits whose areas are listed in Table V. These were calculated from the formula

$$m^*=\frac{1}{\pi}\oint_{\text{orbit}}\frac{d\mathbf{k}}{d\mathcal{E}}=\frac{1}{\pi}\frac{dA}{d\mathcal{E}}. \tag{8}$$

For the nonlocal model the energy differential $d\mathcal{E}$ was explicitly included in the matrix elements of the Hamiltonian. The masses which were obtained are tabulated in Table V.

On the average, the masses obtained for the local model were 30% smaller than experimental masses while those obtained from the nonlocal model averaged 26% smaller. One would normally describe this difference by an enhancement factor. This enhancement factor is listed in Table V as a percentage deviation for each mass. The enhancement factors for the local model vary from about 20 to 33%; the enhancement factors for the nonlocal model vary from about 20 to 30%. These enhancement factors would normally be at-

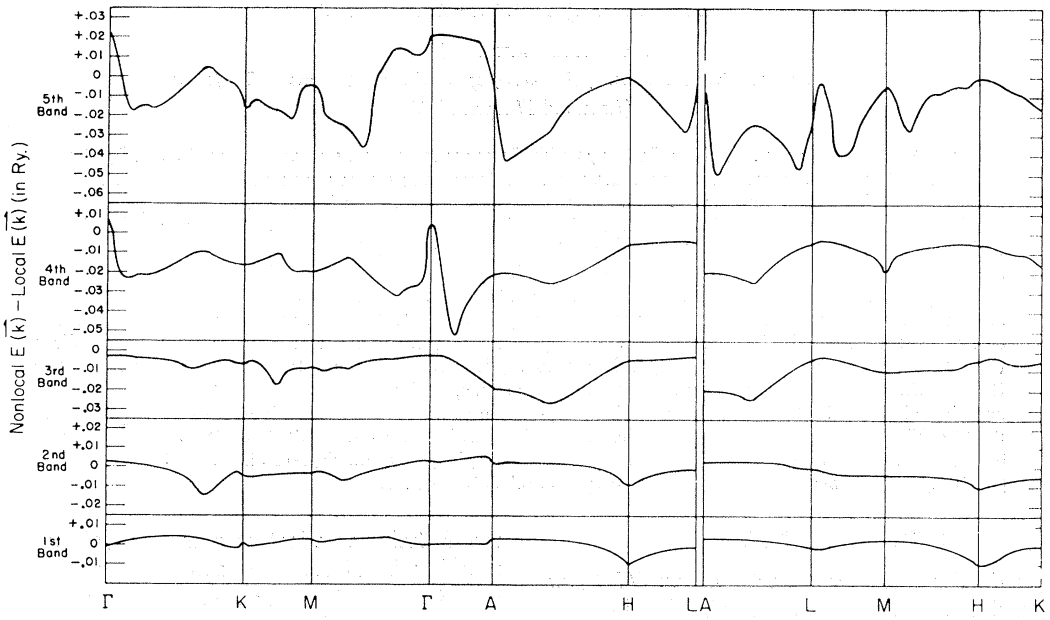

FIG. 10. The difference $\mathcal{E}(\mathbf{k})_{\text{nonlocal}}-\mathcal{E}(\mathbf{k})_{\text{local}}$ for the lowest five energy bands along the major symmetry lines of the Brillouin zone. The lowest band is labeled 1, the second lowest is labeled 2, etc.

tributed to electron-electron[15] and electron-phonon[16] interactions. Thus any significant variation in the enhancement factor within each model would appear to indicate that these interactions are **k** dependent. The variations shown in Table V probably only reflect the uncertainty in the experimental masses. The only conclusion which we can draw with any confidence from the data listed in Table V is that the nonlocal model requires only about $\frac{3}{4}$ as much enhancement as the local model. The nonlocal model should give the more realistic value for the enhancement since the energy dependence of the matrix elements is ignored in the local model.

It is interesting to note that the local pseudopotential masses are on the whole nearly identical to the single OPW masses. Thus the average 30% enhancement found for this model indicates a 30% increase in the density of states at the Fermi level relative to the free-electron bands. The electronic specific-heat data[17] yields a value of 1.33 for the density of states relative to the free electron, which is in good agreement with our calculated average.

[15] T. M. Rice, Ann. Phys. (N. Y.) **31**, 100 (1965).
[16] N. W. Ashcroft and J. W. Wilkins, Phys. Letters **14**, 285 (1965).
[17] J. G. Duant, in *Progress in Low-Temperature Physics*, edited by C. J. Gorter (North-Holland Publishing Company, Amsterdam, 1955), p. 210.

CONCLUSIONS

A polyvalent metal such as magnesium which has Fermi surface sheets in several Brillouin zones offers a demanding test of the accuracy of any model-Hamiltonian band-structure representation. Magnesium is an element particularly suited for this test since it has a tightly bound core with a closed-shell configuration. This is the case for which the cancellation theorem should apply. The local and nonlocal pseudopotential calculations reported in this paper yield accurate models for the magnesium Fermi surface. These models should be viewed primarily as an interpolation procedure whereby one generates the entire Fermi surface from data limited to only portions of the Fermi surface. Insofar as the single-particle approximation is valid, these models also generate the entire band structure for energies other than E_F.

Comparisons of the models with the experimental data indicate that the errors in the local pseudopotential are about $\pm 3\times 10^{-3}$ Ry, while we could find no errors in the nonlocal pseudopotential model greater than our truncation error of $\pm 1.5\times 10^{-3}$ Ry. We can conclude from this that while the local pseudopotential model offers a very accurate representation of the magnesium Fermi surface, the most accurate fit to the data can only be achieved by inclusion of the nonlocal nature of the pseudopotential.

PHYSICAL REVIEW VOLUME 162, NUMBER 3 15 OCTOBER 1967

Magnetic Ordering in Dilute Solid Solutions of Iron in Gold. II. Electric Hyperfine Interactions*

C. E. VIOLET AND R. J. BORG
Lawrence Radiation Laboratory, University of California, Livermore, California
(Received 17 April 1967)

The Fe^{57} Mössbauer spectra of Au-Fe alloys with Fe concentrations between 1.7 and 10.5 at.% at temperatures between the transition temperature and room temperature consist of a doublet superimposed on a central line which is an unresolved doublet. The centroids of the two doublets are separated by 0.06±0.02 mm/sec. This is independent of Fe concentration and temperature. The outer doublet is associated with Fe ions with one or more Fe nearest neighbors, while the inner doublet is associated with Fe ions with no Fe nearest neighbors. The separation of the outer doublet lines is independent of Fe concentration and is 0.77±0.02 mm/sec at 77°K and 0.69±0.02 mm/sec at 294°K. The separation of the inner doublet is an order of magnitude smaller. It increases with increasing Fe concentration, but has no detectable dependence on temperature. These doublets are interpreted as quadrupole-split resonance lines. The electric field gradient (EFG) of the outer doublet probably arises from conduction electrons within the atomic sphere. The EFG of the inner doublet may arise from random strains, or Fe impurity charges beyond the nearest-neighbor shell, or both. An analysis of the temperature shifts gives an effective Debye temperature of (290±40)°K for Fe impurities in Au. The observed linewidths are independent of Fe concentration and temperature from 77 to 294°K. The linewidths increase slightly at a few degrees above the transition temperature, perhaps because of the onset of magnetic-relaxation effects.

I. INTRODUCTION

IN a previous paper[1] (henceforth called VB-1) we presented the results of an investigation in which the Mössbauer effect was used to observe magnetic ordering in dilute solid solutions of Fe in Au. The magnitude of the hyperfine splitting was studied as a function of composition and temperature, and the magnetic transition temperature (T_0) was determined as a function of composition. Spectra were obtained for

* Work performed under the auspices of the U. S. Atomic Energy Commission.
[1] C. E. Violet and R. J. Borg, Phys. Rev. **149**, 540 (1966).